PZT Nanofilm-Based, Wafer Scale Nanoresonators

Denis Dezest, Fabrice Mathieu, Laurent Mazenq, Liviu Nicu
LAAS-CNRS
University of Paul Sabatier, Toulouse
Toulouse, France

Caroline Soyer, Jean Costecalde, Olivier Thomas, Denis Remiens
IEMN-CNRS
University of Lille Nord de France
Lille, France

***Abstract*— In this work, we present an unprecedented level of integration of piezoelectric actuation means on arrays of functional nanoresonators at the wafer scale. We use 150-nm thin lead titanate zirconate (PZT) as piezoelectric material mainly because of its excellent actuation properties even when geometrically constrained at extreme scale. This work paves promising ways for NEMS to be used in configurations where transduction capabilities are integrated at the nanodevice level providing effective fabrication process flow at the wafer-scale.**

Keywords—NEMS, actuators, piezoelectric actuation, PZT

I. INTRODUCTION

For nanoelectromechanical systems (NEMS) to start being a viable alternative to their microscale counterparts (i.e. microelectromechanical systems or MEMS), the fully integrated transduction at the wafer scale represents the ultimate goal to be achieved. By integrated transduction one means both actuation and sensing of movement capabilities of freestanding nanostructures. So far, relevant results in that sense have been obtained at the chip level either by transposing traditional transduction schemes at the nanoscale [1,2] or delivering brand new schemes exclusively adapted to the NEMS realm [3]. Recent efforts to demonstrate full-wafer NEMS with integrated transduction means have been done [4, 5] but remain rather seldom which demonstrates how critical the gap between chip and wafer scale is.

In this work, we demonstrate the integration of piezoelectric actuation means on arrays of nanocantilevers at the wafer scale. We use lead titanate zirconate (PZT) as piezoelectric material mainly because of its excellent actuation properties even when geometrically constrained at extreme scale [6].

II. FABRICATION

A. Design

Chips (16 mm x 16 mm) of 256 silicon-based cantilevers have been fabricated from a 4 inches silicon-on-insulator (SOI) wafer. Resonators with different sizes and geometries have been implemented. The beams' width has been varied from 1.6 µm to 5 µm and the length from 6 µm to 12 µm. A multilayer stack composed of a 150-nm thick PZT ($PbZr_{0.54}Ti_{0.46}O_3$) thin film sandwiched between a 100-nm thick lanthanum nickelate ($LaNiO_3$ or LNO) bottom electrode and a 12/120-nm thick titanium/platinum (Ti/Pt) top electrode serves as the integrated piezoelectric transducer. Two different geometries for the piezoelectric stack have been implemented. In geometry A, the piezoelectric stack transducer covers almost the full length of the resonator and each layer of the stack is completely covered by the upper layer. In geometry B, half-length of the cantilever is covered by the piezoelectric stack for which both the bottom and top electrodes have the same dimensions. The resonators are divided into 64 arrays of 4 cantilevers with the same width but with varying lengths and with the same geometry. Optical and SEM pictures of the devices are shown in Fig. 1.

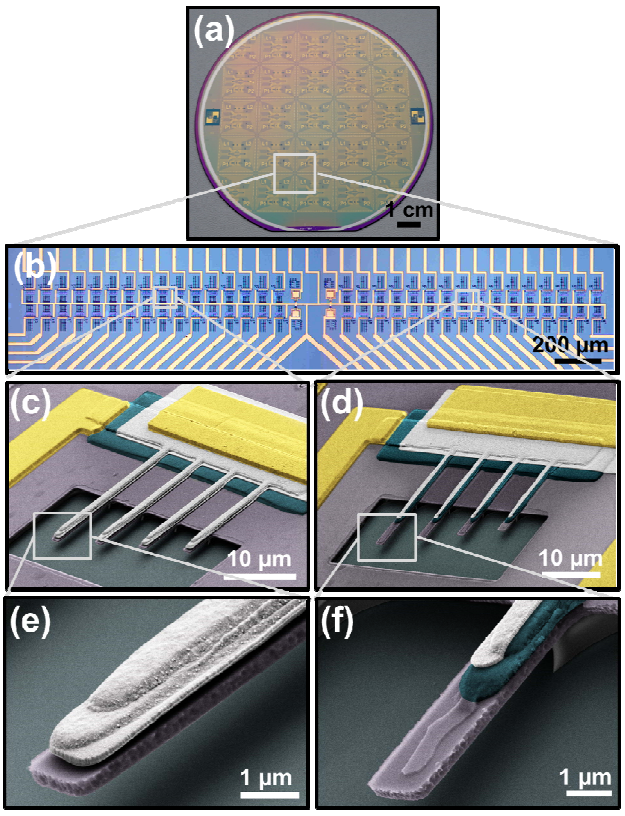

Fig. 1. (a) Wafer-scale fabrication of NEMS cantilevers on a 4 inches SOI wafer. (b) Each chip is composed of 64 arrays of 4 cantilevers. Colored scanning electron microscope (SEM) pictures of 2 arrays of 2.4 µm wide cantilevers with geometries A and B are respectively shown in (c) and (d). The color code use is the same for the figures 1, 2 and 4. A close view of the two configurations for the multilayer stack is shown in (e) and (f).

B. Fabrication

The fabrication method was performed on SOI 4" P-type (100) wafer (340nm/1µm/525µm). Arrays of four cantilevers of different lengths (from 2µm to 10.5µm) and similar width have been placed on the wafer. The width was varied from 1µm to 2.8µm. A piezoelectric stack including top Ti-Pt (12-120nm thick) and bottom LNO (100nm thick) electrodes as well as the PZT material (150nm thick) has been patterned on each nanocantilever in two covering configurations: full-length or half-length of the nanocantilever. The elastic support beneath the piezoelectric stack was made of the SOI device silicon layer covered by a 30nm thick thermal silicon dioxide. The whole fabrication process was performed at the wafer scale, the lithography steps being realized using a UV stepper photo repeater (CANON FPA 3000i4/i5).

First, a 30 nm-thick layer of SiO2 is thermally grown to serve as an electrical insulation layer. Both thermal oxide and silicon device layers are then successively etched (AMS4200 Alcatel Inc.) by reactive ion etching (RIE) to pattern the shape of the structures. Collective integration of the piezoelectric stack onto individual structures starts with the deposition of the bottom electrode. A 100 nm-thick layer of LNO is sputtered and patterned on the structures by lift-off using a high-resolution bi-layers positive photoresist LOR3A/ECI3012 (purchased from MicroChemicals, Germany). LNO acts as a diffusion barrier against lead atoms migration during the PZT crystallization step. It prevents lead atoms to diffuse and react with any underlying Si-based material. A low-temperature RF-magnetron sputtering deposition compatible with lift-off patterning is then used to define a 150 nm-thick active layer of PbZr0.54Ti0.46O3 (PZT 54/46) [6]. This composition is close to the morphotropic phase boundary (MPB) where PZT exhibits optimal piezoelectric and dielectric properties [7]. PZT patterning by lift-off is an alternative approach to conventional dry and wet etching techniques. The former has been reported to deteriorate the PZT material properties due to a combination of both physical damages and chemical contaminations [8,9] while the latter requires using HF solution which can be incompatible with other etchant-sensitive materials and suffers from undesirable undercut of masked features. After deposition, a mandatory annealing at 625°C for 30 min is performed to crystallize the PZT into the perovskite phase. A 12/120 nm-thick layer of Ti/Pt is then deposited and patterned by lift-off as the top electrode. Each array of structures is then individually addressed with 100/700 nm-thick Ti /Au interconnections. The structures are released by wet etching of the sacrificial layer after a photoresist encapsulation to protect other sensitive layers. We use a 2.6 µm-thick ECI 3012 positive photoresist (purchased from MicroChemicals, Germany) with an additional baking at 115°C for 1 min before etching to enhance the photoresist adhesion. A buffered oxide etchant (BOE) composed of 7-1 ratio of ammonium fluoride (NH4F) – hydrofluoric acid (HF) mixture with an isotropic etch rate of around 77 nm/min is used at room temperature to release the structures. Two subsequent wet etching – photoresist encapsulations are performed to reduce photoresist adhesion defects due to long etching time while being able order to release the largest structures up to 5 µm wide. Nevertheless, this critical step imposes the final yield (around 33 %) of the implemented fabrication process.

C. Experimental set-up

The actuation of the resonators is performed according two different configurations: external actuation (off-chip) and integrated actuation (on-chip). In the former the chip is mounted onto a piezodisk electrically driven by a network analyzer, as shown on Fig. 2(a). Resonators are therefore collectively actuated through the piezoshaker and individually read-out. In the latter configuration, the chip is glued to a metalized polyimide support with dedicated gold-wiring interconnections. Devices of a same array are then self-actuated by biasing the top and bottom electrodes (see Fig. 2(b)) with a network analyzer.

For both actuation configurations, the mechanical motion of individual cantilever is optically read-out by a home-made Fabry-Perot interferometer bench. In this setup, a chip is clamped on a motorized piezoelectric precision stage (XYZ translations) inside a vacuum chamber pumped down to a secondary vacuum (around 10-6 mbar) at room temperature. A 30 mW helium-neon (of wavelength $\lambda = 633$ nm) laser is focused through a beam expander (X5) onto the surface of a resonator and a long working distance microscope objective (20X, N.A. 0.28). The fine positioning of the laser is controlled by the piezo-stage displacement while the operation is monitored with a CMOS camera under a LED blue light ($\lambda = 470$nm). The air gap between the suspended resonator and the substrate underneath acts as a Fabry-Perot cavity. Mechanical oscillations of the driven resonator affect the gap size of the optical cavity and modulate the intensity of the interferences between the multiple reflected beams. The intensity of the reflected optical signal is modulated at the driving frequency and its amplitude is proportional to the resonator displacement. Details of the the Fabry-Perot interferometry principle used as a sensing technique for MEMS have been described by Carr and Craighead [10]. The optical signal is reflected back through the microscope objective and diverted through a beamsplitter toward an AC coupled photodetector (New Focus model 1601). The photodetector AC output is connected to the network analyzer (Agilent model 4395A) to track the mechanical response of the resonator at the frequency of the excitation signal similarly to a lock-in amplifier detection.

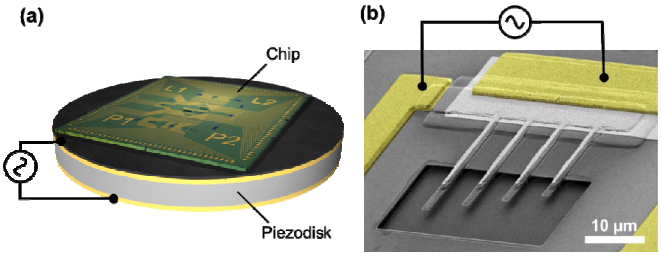

Fig.2: The two actuation configurations external (off-chip) and integrated (on-chip) are respectively shown in (a) and (b).

III. Q-FACTOR VERSUS AIR PRESSURE

Performance of resonating structures generally suffer from many dissipative mechanisms [11] which affect both the amplitude and the sharpness of the peak resonance. Dissipation, defined as the inverse of the quality factor ($D = Q^{-1}$), is a measure of the mechanical energy lost per cycle of the oscillation (it is the ratio of this lost energy over the total energy stored in the resonator). Any dissipation mechanism can be described as an additional and uncorrelated linear force proportional to the resonator velocity that resists motion. Since no correlation exists between the dissipation sources, the total dissipation within a system is defined as the sum of all the dissipative contributions:

$$Q^{-1} = \sum_i Q_i^{-1} \quad (1)$$

For biosensing [12] applications, resonators are operated in gaseous or liquid media for which viscous damping is usually the dominant source of dissipation. We have investigated the effect of pressure on the quality factor for structures with a multilayer stack. Measurements are performed according to the following manner. The chamber is pumped down to a pressure of 1.1×10^{-6} mbar after which measurements of the quality factor are carried out up to atmospheric pressure. A leak valve is used to flow nitrogen inside the chamber while monitoring the vacuum level with a pressure gauge (Inverted magnetron Pirani gauge model FRG-700, Agilent Inc.). The pressure gauge is actually a combination of two measurement systems (Pirani and cold cathode) with a measuring range from 5×10^{-9} mbar to atmospheric pressure and an accuracy of ± 30 %. Measurements of the quality factor are performed after the pressure is stabilized while the pumps are still on. Then the pumps are switched off during measurements and the pressure starts to slightly increase toward atmospheric pressure. Results obtained for the fundamental resonant mode of a cantilever with geometry C8 are shown in Fig.3. The Knudsen number K_n defined as the ratio between the mean free path λ of gas molecules and the cantilever width w is plotted on the top axis.

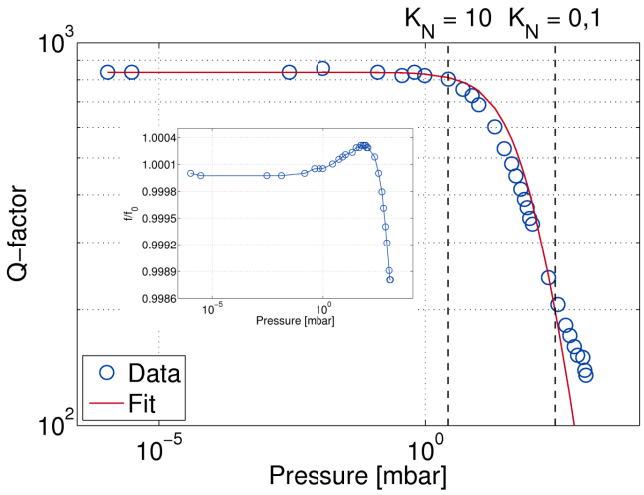

Fig.3: Pressure dependence of the quality factor for a multilayer stack suspended cantilever with geometry C8 for the fundamental flexural mode. Experimental data (blue square symbols) are fitted with a theoretical model (pink solid line) based on the free molecular regime taking into account the squeeze-film damping (Q_{FM}). A vertical dashed line drawn at $K_n = 10$ indicates the separation between the intrinsic and the molecular regime. Another vertical dashed line at $K_n = 0.1$ pinpoints the crossover between the molecular and viscous regimes. The relative variations of the resonant frequency f compared to the resonant frequency in vacuum f_0 plotted versus the increasing gas pressure are shown in the inset.

Extrinsinc damping due to a surrounding medium is generally described by three different regimes [13]. At low pressures ($K_n > 10$) in the so-called intrinsic regime, dissipation is mainly dominated by intrinsic and pressure-independent mechanisms (losses within the material itself). A value of 837 for the quality factor is experimentally measured at the lowest pressure and is set as the $Q_{intrinsic}$ value. Higher pressures ($0.1 < K_n < 10$) correspond to the free molecular regime in which energy loss due to momentum transfer between individual gas molecules and the resonating structure becomes the dominant dissipation mechanism. For suspended structure an additional dissipation term relative to squeeze-film damping has to be added to take into account the presence of an air gap between the resonator and the substrate [14]. The total dissipation (1) becomes in this regime:

$$Q_{FM}^{-1} = Q_{intrinsic}^{-1} + Q_{molecular}^{-1} + Q_{squeeze}^{-1} \quad (2)$$

As shown in Fig.3, data are in a fair agreement with the prediction regarding the accuracy of the pressure gauge and in spite of the complexity of the multilayer stack resonator. A deviation from the model occurs at a pressure of around 265 mbar ($K_n = 0.1$) due to the crossover between the molecular and the continuum regimes. The Knudsen number relative to this demarcation is in the same range of values [0.1-0.7] reported elsewhere [15,16]. In the continuous regime gas molecules have to be considered as a viscous incompressible fluid with a mean free path smaller than the cantilever's width. However none of the existing models for the viscous regime [13,14,17] are suitable for the non-homogenous geometry of the fabricated cantilevers and are therefore not presented here.

The resonant frequency of the cantilever decreases as expected with the increasing gas pressure. As the cantilever vibrates in a gaseous environment, it pushes away an amount of air around it that is generally described by an added mass. However the total shift of the resonant frequency from vacuum to air is relatively small (0.12 %). It worth noticing that a slight increase is observed in the crossover region between the molecular and viscous regimes prior to the global dropping of the resonant frequency. Such phenomenon has been reported elsewhere [18] but is not yet fully understood.

IV. Estimation of the Limit of Detection

For applications such as mass sensing, the limit of detection (LOD) of the system is one of the key features to evaluate its performance. For a beam loaded with a small added mass δM uniformly distributed over its surface, the shift in the natural frequency is given by [19]:

$$\delta f = -\frac{\delta M}{2M_2} f_0 \tag{3}$$

where δf is the resonant frequency shift due to the added mass δM and f_0 is the natural frequency. In this case, the effective mass M_2 is defined as follows:

$$M_2 = \frac{L\int_0^L m(x)\Phi^2(x)dx}{\int_0^L \Phi^2(x)dx} \tag{4}$$

In the case of a uniform beam, the effective mass is clearly equal to the total mass of the beam. However, in the present case of a laminated beam with a non-uniform mass density, it is found to be equal to a fraction of the total mass of the beam and is computed by the FE model. The LOD is therefore defined as the smallest added mass δM_{min} producing the smallest measurable shift δf_{min} in the natural frequency: $LOD = \delta M_{min}$.

Experimentally the LOD of a resonator can be obtained by monitoring the nominal resonant frequency f_0 (or phase variations) over a certain period of time and computing the Allan deviation $\sigma_{Allan}(\tau)$, square root of the Allan variance. It is an estimator of the true mathematical variance and corresponds to an IEEE standard [20] commonly used to characterize the frequency stability of an oscillator in the time domain. For a finite data set of N values of instantaneous frequencies $f_i(t)$ measured with a sample rate τ_0, normalized frequency deviations can be defined according to:

$$\bar{y}_i^{\tau_0} = \frac{f_i(t) - f_0}{f_0} \tag{5}$$

A different data set of normalized frequency deviations can be obtained by changing the sampling time to $\tau = m\tau_0$ (with m a positive integer) and averaging m adjacent values of $\bar{y}_i^{\tau_0}$ to obtain a new estimate [21]:

$$\bar{y}_k^{\tau} = \frac{1}{m}\sum_{i=k}^{k+m-1} \bar{y}_i^{\tau_0} \tag{6}$$

The Allan variance with overlapping is usually preferred to the standard Allan variance (also known as the two-sample variance) since more sample data are available for the variance calculation, leading to a better confidence interval and therefore a more reliable estimator. The expression for the estimator of the Allan variance with overlapping is given by [21]:

$$\sigma_{Allan}^2(\tau) = \frac{1}{2(N-2m+1)}\sum_{k=1}^{N-2m+1} (\bar{y}_{k+m}^{\tau} - \bar{y}_k^{\tau})^2 \tag{7}$$

Where $\bar{y}_{k+m}^{\tau}$ and $\bar{y}_k^{\tau}$ are adjacent (i.e.with no dead time between the measurements) normalized frequency deviations, averaged over the sample rate $\tau = m\tau_0$.

The resonant frequency for a cantilever with geometry C8 was monitored over a total time of around 300 s with a measurement sample rate of $\tau_0 = 0.216$ s in primary vacuum (10^{-1} mbar) at room temperature (24 °C) under a driving amplitude of 100 mV. The computed Allan deviation is shown in Fig.4.

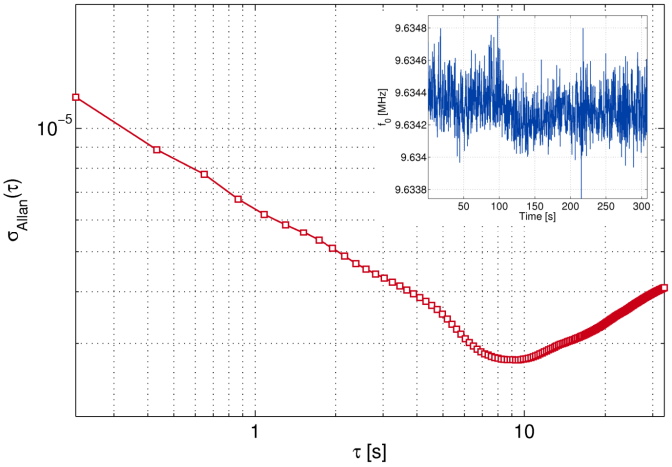

Fig.4: Allan deviation with overlapping obtained for a cantilever with geometry C8 computed for integration times between 0.216 s and 33 s. The resonant frequency was monitored over 300 s (inset) in vacuum at room temperature for a driving amplitude of 100 mV.

The minimum measured Allan deviation if found to be equal to $\sigma_{Allan}(\tau) \approx 2.74 \times 10^{-6}$ for a sample time of $\tau \approx 9.29$ s which yields according to equation (3) to: $LOD = \delta M_{min} \approx 106$ ag. It is common for comparison purposes to express the LOD relatively to the surface of the resonator. The so-called surface mass limit of detection (SMLOD) is therefore: $SMLOD \approx 5\ \mathrm{ag.\mu m^{-2}}$.

V. Conclusion

Collective fabrication at the wafer-scale of self-actuated cantilever-based resonators with an integrated 150 nm-thick PZT thin film has been reported. Standard surface micromachining technologies such as UV lithography appear as a good compromise between the degree of miniaturization

and high-throughput manufacturing of resonators with integrated transduction means. Dynamic mechanical characterization of the fabricated cantilevers with different geometries has shown a preserved mechanical integrity and a dynamic behavior in a fair agreement with the finite element analysis. Quality factor values of ~900 in a vacuum and ~130 in air have been obtained at room temperature for fundamental resonant responses in the megahertz range. Piezoelectric actuation capabilities were validated in the linear regime for the first time at this integration level in spite of a low piezoelectric constant probably due to the lateral confinement. Discussion on the piezoelectric sensing shows how critical the transition from the micro-scale to the nano-scale is. This work shows promise and paves the way for further research dedicated to the NEMS realm to address the challenge of the transduction integration at the nano-scale to provide fabrication at the wafer-scale.

ACKNOWLEDGMENT

The French General Delegation for Armament and the French National Agency for Research (grant ANR/PNANO 2008, project NEMSPIEZO 'ANR-08-NANO-015') are gratefully acknowledged for financial support.

REFERENCES

[1] L. G. Villanueva, R. B. Karabalin, M. H. Matheny, E. Kenig, M. C. Cross, M. L. Roukes, "A Nanoscale Parametric Feedback Amplifier", Nano Letters, vol. 11, pp. 5054-5059, 2011.

[2] M. Li, H. X. Tang, M. L. Roukes, "Ultra-Sensitive NEMS-based Cantilevers for Sensing, Scanned Probe and Very High-Frequency Applications", Nat. Nanotechnol., vol. 2, pp. 114-120, 2007.

[3] Q. P. Unterreithmeier, E. M. Weig, J. P. Kotthaus, "Universal Transduction Scheme for Nanomechanical Systems Based on Dielectric Forces", Nature, vol. 458, pp. 1001-1004, 2009.

[4] J. Arcamone, M. A. F. van den Boogaart, F. Serra-Graells, J. Fraxedas, J. Brugger, F. Perez-Murano, "Full-Wafer Fabrication by Nanotencil Lithography of Micro/Nanomechanical Mass Sensors Monolithically Integrated with CMOS", Nanotechnology, vol. 19, 305302, 2008.

[5] I. Bargatin, E. B. Meyers, J. S. Aldridge, C. Marcoux et al., "Large-Scale integration of NEMS for Gas Sensing Applications", Nano Letters, vol. 12, pp. 1269-1274, 2012.

[6] S. Guillon, D. Saya, L. Mazenq, J. Costecalde, D. Remiens, C. Soyer, L. Nicu, "Lead Zirconate Titanate Nanoscale Patterning by UV-based Lithography Lift-Off Technique for Nano-Electromechanical Systems Applications", IEEE Trans. On Ultrasonics Ferroelec. Freq. Control, vol. 59, pp. 1955-1961, 2012.

[7] H.D. Chen, K.R. Udayakumar, C.J. Gaskey, L.E. Cross, "Electrical properties' maxima in thin films of the lead zirconate–lead titanate solid solution system", Appl. Phys. Lett. Vol.67, pp. 3411-3413, 1995

[8] C.W. Chung, C.J. Kim, "Etching Effects on Ferroelectric Capacitors with Multilayered Electrodes", Japanese J. Appl. Phys., vol. 36, pp.2747-2753, 1997

[9] K.T. Kim, M.G. Kang, C.I. Kim, "Study on the etching damage characteristics of PZT thin films after etching in Cl-based plasma", Microelectron. Eng., vol.71, pp. 294-300, 2004

[10] D.W. Carr, H.G. Craighead, "Fabrication of nanoelectromechanical systems in single crystal silicon using silicon on insulator substrates and electron beam lithography", J. Vac. Sci. Technol. B, vol. 15, pp.2760-2763, 1997

[11] M. Imboden and P. Mohanty, "Dissipation in nanoelectromechanical systems", Phys. Rep., vol. 534, pp. 89–146, 2014

[12] Y. Roupioz, N. Berthet-Duroure, T. Leïchlé, J. B. Pourciel, P. Mailley, S. Cortes, M. B. Villers, P. N. Marche, T. Livache, L. Nicu, "Individual blood-cell capture and 2D organization on microarrays", Small, vol. 5, pp. 1493-1497, 2009

[13] W. E. Newell, "Miniaturization of Tuning Forks", Science, vol. 161, pp. 1320–1326, 1968

[14] C. Bergaud, L. Nicu, A. Martinez, "Multi-mode air damping analysis of composite cantilever beams", Japanese J. Appl. Phys. Part 1, vol. 38, pp. 6521-6525, 1999.

[15] M. Li, H. X. Tang and M. L. Roukes, "Ultra-sensitive NEMS-based cantilevers for sensing, scanned probe and very high-frequency applications", Nat. Nanotechnol. vol. 2, pp. 114–120, 2007

[16] M. Li, R. B. Bhiladvala, T. J. Morrow, J. A. Sioss, K. K. Lew, J. M. Redwing, C. D. Keating and T. S. Mayer, "Bottom-up assembly of large-area nanowire resonator arrays", Nat. Nanotechnol., vol. 3, pp. 88–92, 2008

[17] J. E. Sader, "Frequency response of cantilever beams immersed in viscous fluids with applications to the atomic force microscope", J. Appl. Phys. vol. 84, pp. 64-76, 1998

[18] K. B. Gavan, J. Van der Heijden, E. W. J. M. Van der Drift and H. S. J. Van der Zant, "Effect of pressure on the Q factor and the resonance frequency of SiN microcantilevers", 4th IEEE International Conference on Nano/Micro Engineered and Molecular Systems, pp. 380–3844, 2009

[19] K. L. Ekinci, Y. T. Yang and M. L. Roukes, "Ultimate limits to inertial mass sensing based upon nanoelectromechanical systems", J. Appl. Phys., vol. 95, pp. 2682-2689 , 2004

[20] J. A. Barnes, A. R. Chi, L. S. Cutler, D. J. Healey, D. B. Leeson, T. E. McGunigal, J. A. Mullen, W. L. Smith, R. L. Sydnor, R. F. C. Vessot and G. M. R. Winkler, "Characterization of Frequency Stability", IEEE Trans. Instrum. Meas., vol. IM-20, pp. 105–120, 1971

[21] D. W. Allan, "Time and Frequency (Time-Domain) Characterization, Estimation, and Prediction of Precision Clocks and Oscillators", IEEE Trans. Ultrason. Ferroelectr. Freq. Control, vol. 34, pp. 647–54, 1987